Received: 12 November 2020 | Revised: 8 December 2020 | Accepted: 16 December 2020

High Voltage

DOI: 10.1049/hve2.12067

国家电网 STATE GRID 中国电力科学研究院有限公司 CHINA ELECTRIC POWER RESEARCH INSTITUTE | The Institution of Engineering and Technology | WILEY

ORIGINAL RESEARCH PAPER

Ionization waves in nanosecond pulsed atmospheric pressure plasma jets in argon

Bangdou Huang[1] | **Cheng Zhang**[1,2] | **Wenchao Zhu**[3] | **Xinpei Lu**[4] | **Tao Shao**[1,2]

[1]Beijing International S&T Cooperation Base for Plasma Science and Energy Conversion, Institute of Electrical Engineering, Chinese Academy of Sciences, Beijing, China

[2]University of Chinese Academy of Sciences, Beijing, China

[3]State Key Laboratory of NBC Protection for Civilian, Beijing, People's Republic of China

[4]State Key Laboratory of Advanced Electromagnetic Engineering and Technology, Huazhong University of Science and Technology, Wuhan, Hubei, China

Correspondence

Cheng Zhang, Beijing International S&T Cooperation Base for Plasma Science and Energy Conversion, Institute of Electrical Engineering, Chinese Academy of Sciences, Beijing 100190, China.

Tao Shao, Beijing International S&T Cooperation Base for Plasma Science and Energy Conversion, Institute of Electrical Engineering, Chinese Academy of Sciences, Beijing, China.
Email: st@mail.iee.ac.cn

Associate Editor: Dong Dai

Funding information

National Natural Science Foundation of China; National Science Fund for Distinguished Young Scholars

Abstract

Typical ionization waves (IWs) are observed during the propagation of nanosecond pulsed atmospheric pressure plasma jets (APPJs) with argon flow, combining both the measurement of the axial electric field (E_z) and the temporal resolved optical imaging. The movement of the luminous APPJ head is recognized as the development of the IW front, accompanied with the propagation of the peak electric field. Especially, the radial distribution of E_z transits from a central peak profile before the IW front arrives to a hollow profile after the pass of the IW front. As for the temporal E_z trend, there is a mode transition from the single-peak feature under a low peak voltage to the double-peak feature under a higher peak voltage, indicating the existence of both primary and secondary IWs. The effect of target conditions on the IWs in APPJs is also explored. With a metal target, no residual electric field is observed before imposing the high-voltage pulses. However, with a dielectric target, the residual surface charges generate a background electric field in the opposite direction to that during IW propagation. In the free APPJ (with no target), on the voltage falling edge, a negative electric field drives the electron flow to compensate the positive ions left over during the forward IW propagation on the voltage rising edge.

1 | INTRODUCTION

Atmospheric pressure plasma jet (APPJ) is one of the most engaged discharge forms in the fields of plasma bio-medicine and material treatment, especially when temperature-sensitive targets are concerned [1, 2]. Diffusive and highly reproducible, APPJ has proven its advantage in generating reactive and functional non-thermal plasma in the frequently collisional atmospheric environment [2]. Driving APPJs by means of high-voltage (HV) pulses with a short duration on the order of nanoseconds can further enhance its non-equilibrium characteristic, by generating a large number of high-energy electrons and reactive species, while maintaining both the gas environment and the target material at around room temperature [3].

The formation and functionalization of APPJs are usually accompanied with the propagation of a luminous region in space, which can be revealed using the optical imaging with a nanosecond temporal resolution. This phenomenon is generally called the plasma bullet and indicates the existence of transient processes in APPJs behind their visually stable appearance [2]. In order to explain the discharge propagation during the transient gas breakdown process, the ionization wave (IW), first observed by Thomson in 1893 [4], has been widely adopted [5, 6]. Recently, the concept of ionization wave has been extended to the field of APPJs and it is proposed that a pre-ionized channel with a sufficient seed electron density is important for the formation of highly reproducible APPJs [7, 8]. Even so, the applicability of the IW theory to APPJs is yet to be comprehensively verified.

To inspect the IW mechanism in APPJs, it is essential to know the evolution of the local electric field, which is a key parameter dictating the IW propagation, determining the electron acceleration, and further influencing excitation, ionization, and dissociation processes [6]. The electric field-induced second harmonic (E-FISH) is a recently emerging laser diagnostic technique with a reasonably high spatial–temporal resolution (up to 50 μm and 500 ps, respectively) [9-11]. It has been adopted in different forms of discharges, including diffuse pin-to-plane discharge [12], corona discharge [13], surface dielectric barrier discharge (DBD) [14], fast IW at moderate pressure [15], and APPJs in helium [16].

The E-FISH method provides a non-intrusive approach to explore the propagation mechanism of APPJs, as it is neither limited to the region with detectable luminescence (compared with optical emission spectroscopy (OES) based on the Stark splitting effect [17-19]) nor restricted to the plasma boundary (compared with probes based on the Pockels effect [20]). Furthermore, in the previous investigations related to APPJs mentioned above, a DBD-like (or pin-to-ring) geometry is mostly chosen and APPJs are formed downstream, in which the evolution of the electric field is influenced by a dipole-like source upstream.

Nanosecond pulsed APPJs are operated with a single-electrode geometry in argon flow and the temporal evolution and spatial distribution of the electric field in APPJs is measured using the E-FISH method. Typical structure of the electric field existing in IWs is obtained during the APPJ development. Temporal-resolved optical imaging is used to visualize the IW propagation. The influence of the peak voltage and target configuration is also explored.

2 | EXPERIMENTAL METHODS

Figure 1 shows a schematic diagram of the experimental setup. The discharge gas (argon with a flow rate of 0.5 standard liter per minute for all operation conditions in the study) is blown through a horizontally arranged quartz tube, with an inner diameter of 1.5 mm and an outer diameter of 3 mm, into ambient air. A tungsten pin inside the quartz tube serves as the HV electrode and there is an optional plane target facing the nozzle of the quartz tube perpendicularly. The target can be a grounded copper plate or the same plate covered by Kapton dielectric tape with a thickness of about 200 μm. The free APPJ without a target is also investigated. The distance between the tip of the HV electrode and the nozzle of the quartz tube is around 25 mm, whereas the distance between the target and the nozzle is about 21 mm.

The APPJs under investigation are driven by a customer-made nanosecond pulse generator. The voltage waveform on the HV electrode is measured by a HV probe (VP, Pintech, P6039A) and the current waveform is measured using a current transformer (CT, Pearson, 4100). The pulse repetition rate of the discharge is kept at 1 kHz. Figure 2 shows typical voltage and current waveforms of the APPJs with different target conditions. The zero point of time is defined as when the peak voltage is reached (marked in the voltage waveform). The peak voltage

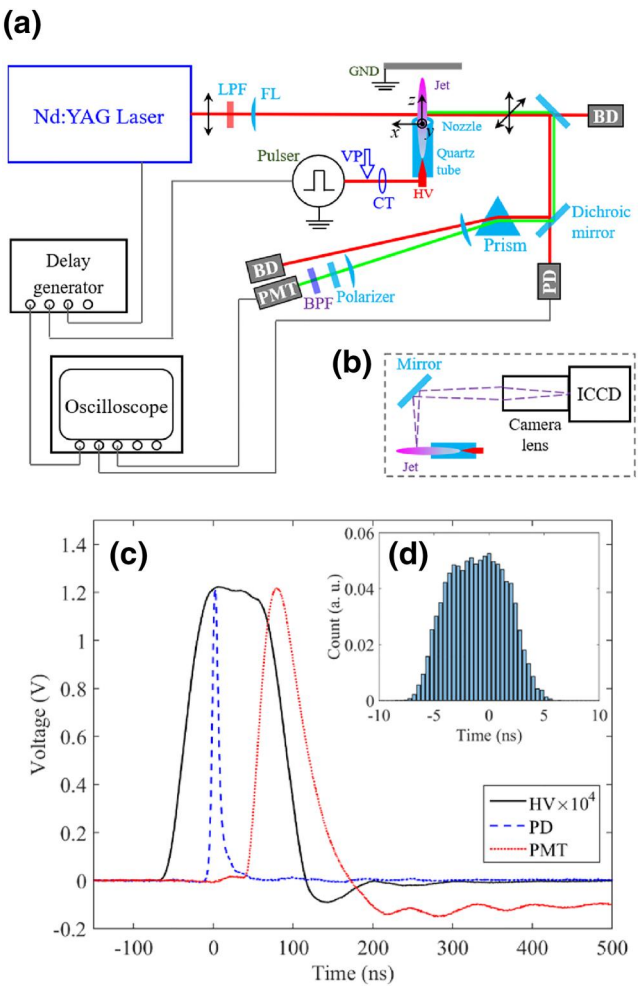

FIGURE 1 A schematic diagram of the experimental setup. (a) the E-FISH system. (b) The optical imaging. (c) Typical waveforms of HV, PD measuring the fundamental laser intensity, and PMT measuring the second harmonic light. (d) The distribution of the time delay between the fundamental laser and the HV pulse. LPF, long pass filter; BPF, band pass filter; FL, focus lens; BD, beam dump; PD, photodiode; PMT, photomultiplier; VP, voltage probe; CT, current transformer

(V_p) can be varied and the time periods for the rising edge, platform, and falling edge are around 50 ns. As for the measured current waveform I_m, there is a positive peak during the voltage rising edge and a negative peak during the voltage falling edge. The displacement current can be obtained from $C_s \times dV/dt$. Here, dV/dt is the time differential of the voltage waveform and C_s is the stray capacitance of the discharge geometry, which can be obtained by applying a lower voltage (below the breakdown threshold) without discharge [21]. The difference between the measured current and the displacement current I_m-$C_s \times dV/dt$ gives the conductive current. It can be seen that the displacement current contributes to the majority of the total current, while the conductive current has a much lower amplitude compared with the displacement current. With a metal target, the conductive current appears when there is a conductive plasma channel formed, i.e. after the head of APPJ touches the target. This argument will be supported by the temporal evolution of the discharge images shown in Figure 3. From

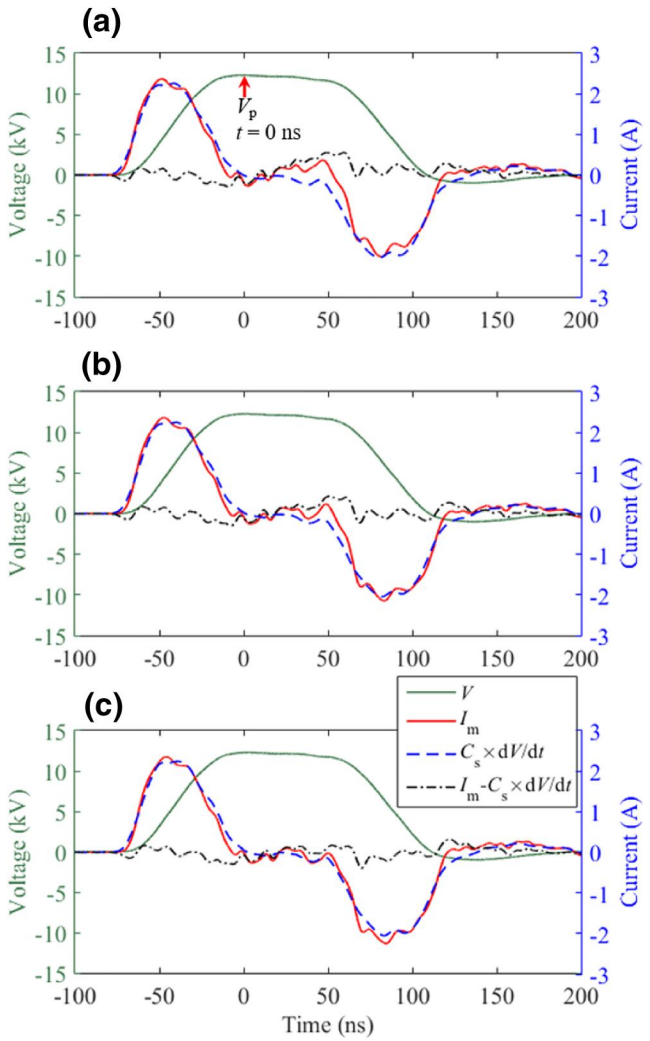

FIGURE 2 Typical voltage and current waveforms of the APPJs with different targets. (a) Metal target, (b) Kapton target, and (c) without target (free APPJ)

Figure 2(a–c), it can be found that the APPJ with a Kapton target has lower conductive current compared with a metal one, and no distinguished conductive current can be observed in the case without a target. Similar effect of target condition on the conductive current has been observed in [22].

In this investigation, the axial electric field (E_z) of the plasma jet outside the tube nozzle is measured using the E-FISH method, which is similar to that in previous studies [14, 23]. Briefly, the 1064 nm fundamental beam of a nanosecond Nd:YAG laser (Beamtech SGR-S400, pulse width 7–9 ns, 10 Hz) is focused to the discharge region using a plano-convex lens (focal length $f \approx 55$ cm). The laser energy is set as 20 mJ per pulse in current work. The measured $1/e^2$ radius of the fundamental laser beam around the focal point is approximately 130 μm, by the traversing knife–edge method. Consequently, the confocal parameter of the fundamental laser b_1 is about 10 cm [14]. The polarization of the fundamental laser is horizontal, i.e. it is in the same direction as the APPJ's axis. After the laser passes through the discharge region, the fundamental laser and the second harmonic light are dispersed in space with a prism. The horizontally polarized component of the second harmonic light is selected using a polarizer and a band pass filter. The intensity of the fundamental laser $I(\omega)$ and that of the second harmonic light $I(2\omega)$ are detected with a photodiode (PD, Thorlabs, DET10A2) and a photomultiplier (PMT, Hamamatsu, R1828-01), respectively.

Figure 1(c) shows typical waveforms of HV, PD, and PMT, recorded by the oscilloscope. The Nd:YAG laser and the nanosecond HV generator are synchronized with a delay generator (SRS, DG645) and the time interval between the laser output and the HV pulse, i.e. the time point for the E_z measurement, can be changed. Signal average over 1000 laser shots is performed for each location and time point. Notice that the peak of PMT signal, coming much later than the PD signal, does not indicate the time when the second harmonic light is generated, limited by the temporal response of the PMT pre-amplifier. The jitter between the fundamental laser and the HV pulse is about 8 ns, indicated by the full width at half maximum (FWHM) of the distribution of the delay between these two signals (as shown in Figure 1(d)), which will further reduce the temporal resolution of the E-FISH measurement, except for the pulse width of the fundamental laser. As a result, the peak value of the electric field could be under-estimated, which is due to that at a certain location, the time period with a strong electric field during IW propagation (when the IW front passes by) can be on the order of nanosecond or even sub-nanosecond [12].

The calibration of the E-FISH system is performed by using a parallel-plate electrode geometry, with a width of about 12 mm and a gap of about 2.5 mm, which is the same as our former work [14]. By applying a sub-breakdown voltage, a known and uniform electric field E_0 is generated, with the interaction length between the fundamental laser and electric field $L \approx 12$ mm. Under the condition with a uniform electric field distribution, the intensity of the second harmonic light $I(2\omega)$ can be given by [12].

$$I(2\omega) \propto \left[N \chi^{(3)} E_0(\omega_0)\, I(\omega)\, L\right]^2 \left[\frac{\sin(\Delta k \cdot L/2)}{\Delta k \cdot L/2}\right]^2 \qquad (1)$$

Here, N is the density of neutral gas. $\chi^{(3)}$ is the third-order non-linear susceptibility (hyperpolarizability). $E_0(\omega_0)$ indicates the external electric field, whose frequency ω_0 is much lower than the laser frequency ($\omega >> \omega_0$). Δk is the wavevector mis-match between the fundamental laser and the second harmonic light. The detection limit of the current system, expressed using the product of external electric field strength and laser-electric field interaction length $E_0 \cdot L$ is on the order of 0.5 (kV/cm)·cm, taking the contribution of emission from the discharge, stray light from the laser, and electro-magnetic interference into consideration.

Except for the E-FISH measurement, the temporal evolution of the discharge images is also obtained by using a camera lens and an intensified charge coupled device (ICCD, Andor, iStar-sCMOS18U73), as illustrated in Figure 1(b).

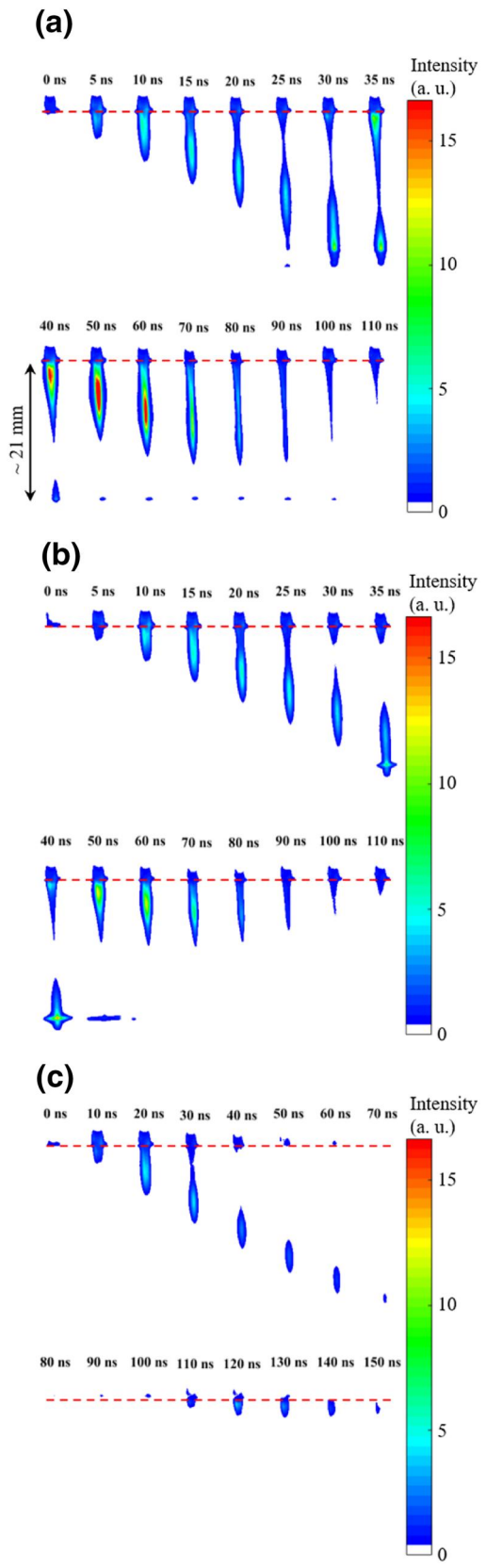

FIGURE 3 The temporal evolution of the images of the APPJs with different targets and with a peak voltage of about 12 kV taken by ICCD camera: (a) metal target (1800 pulses for each frame), (b) Kapton target (4000 pulses), (c) free APPJ without target (4000 pulses)

3 | RESULTS AND DISCUSSION

Figure 3 shows the temporal evolution of the discharge images with different target conditions taken by the ICCD camera, i.e. (a) metal target, (b) Kapton target, and (c) no target. The gate width is 5 ns and each frame is accumulated over multiple pulses. The time point above each image indicates the starting time of the ICCD gate. The red dashed line in these figures indicates the location of the nozzle of the quartz tube ($z = 0$ in the axial direction). Notice that the APPJ propagates vertically in Figure 3, due to a reflection mirror being used when taking the discharge images (indicated in Figure 1(b)).

As shown in Figure 3a, from 0 to 35 ns, the APPJ propagates from the nozzle of the quartz tube to the ground target, indicated by the movement of the luminous head. A dark column is left over after the luminous head passes by, which phenomenon is widely observed in different kinds of APPJs [2, 7]. We call this propagation process the primary ionization wave. Afterwards, from 40 to 75 ns, there is a secondary propagation of the APPJ initialized from the nozzle, indicated by the extension of the bright column (called secondary IW) [24]. Notice that during the propagation of the secondary IW, there is no obvious dark column. In addition, the period of secondary IW formation also corresponds to that when there is noticeable conductive current (shown in Figure 2). The reproducibility of the APPJs in this work is also checked by the optical imaging with the ICCD camera, which shows that the APPJ head reaches a certain position at the same time (in the frame with the same delay) in repetitive measurements.

In the case of APPJ with a dielectric target shown in Figure 3(b), the primary IW propagation process is quite similar as that with a metal target. Even so, the emission intensity during secondary IW propagation process is weaker than the former one, the exitance of the dielectric prevents the formation of a conductive plasma channel and continuous electron heating process. On the other hand, after the primary IW front touches the dielectric surface, there is a surface IW propagation process along the dielectric surface, which is also observed in previous investigations [24].

As for the free APPJ without a target, there is only primary IW propagation process and no obvious secondary IW exists. In addition, the propagation velocity of the free APPJ (primary IW), obtained from the movement of peak emission intensity in space, is also slower than that with a target, i.e. about 0.45 mm/ns· *vs.* 0.7 mm/ns.

As the E-FISH method obtains a line-integrated signal along the laser path, it is worth to investigate the radial distribution of the electric field (assuming a cylindrical symmetry). With the current experimental setup, it is fulfilled by moving the APPJ in the vertical direction (in the y direction) while monitoring the E-FISH signal $I(2\omega)$. When the external electric field has a non-uniform spatial distribution, the built-up process of the E-FISH signal for a focused Gaussian beam can be given by [13, 25],

$$I(2\omega, y) \propto \left| \int_{-\infty}^{\infty} N\chi^{(3)} E_0(\omega_0, x, y) E_1^2(\omega) \frac{\exp(\mathrm{i} \cdot \Delta k x)}{1 + \mathrm{i} \cdot 2x/b_1} \mathrm{d}x \right|^2 \quad (2)$$

Here, E_1 is the electric field of the fundamental laser. Note that, as the argon flow is used to generate the APPJ while air is the surrounding, the different hyperpolarizabilities of argon and air ($\chi^{(3)}$[Ar] and $\chi^{(3)}$[Air], respectively) are taken into consideration, i.e. $\chi^{(3)} = \chi^{(3)}$[Ar] if $r \leq 0.75$ mm and $\chi^{(3)} = \chi^{(3)}$[Air] if $r > 0.75$ mm, with $\chi^{(3)}$[Air]/$\chi^{(3)}$[Ar] ≈ 0.79 [26] and $r = (x^2+y^2)^{0.5}$.

In fact, it is no easy task to retrace the radial distribution of E_z directly from the $I(2\omega)$ distribution, e.g. through Abel inversion, while the extension range of E_z (or how wide E_z spreads) is more concerned. In the current investigation, we use several functions, i.e. Gaussian, exponential, and Lorentzian functions, to fit the measured $I(2\omega)$ distribution. Note that in the case when $I(2\omega)$ has a central dip, the corresponding function with a central dip is used. Similar fitting process has been performed in [27].

Figure 4 shows typical results for the vertical distribution of the E-FISH signal intensity $I(2\omega)$ near the nozzle of the quartz tube (as a representative axial position) at several typical time points, i.e. 10 ns before $I(2\omega)$ peaks, the time point when the peak $I(2\omega)$ is reached, and 45 ns after $I(2\omega)$ peaks. Here, APPJ with a metal target is under investigation. Note that the third time point is actually within the period of secondary IW. Figure 5 shows the radial distribution of E_z from the fitting of measured $I(2\omega)$ using the method described above.

Comparing Figure 4(a) and (b), it can be seen that the $I(2\omega)$ distribution before the peak $I(2\omega)$ is wider than when peak $I(2\omega)$ is reached, with a FWHM of about 7 and 3.5 mm, respectively. Consequently, the FWHM for the radial distribution of E_z decreases from about 7.5 to 3.8 mm, as shown in Figure 5(a) and (b). This means that E_z extends in a broader range before the peak E_z is reached, which is also wider compared with the diameter of the APPJ's tube (≈ 1.5 mm), as well as the luminous region. This is reasonable as the electric field belongs to the long-range interaction, while the optical emission is due to the presence of excited species, the distribution of which is more localized. Note that the peak E_z obtained from the fitting of the same $I(2\omega)$ using different functions has a relative variation of 20–30%. Note that the extend range of $I(2\omega)$ and E_z is much smaller than both the coherence length $L_c = \pi/\Delta k \approx 6.7$ cm and the confocal parameter $b_1 \approx 10$ cm, which confirms the validation of applying E-FISH method to APPJs [25].

In Figure 4(c), it is interesting to find that after the peak $I(2\omega)$, i.e. after the primary IW front passes by, the distribution of $I(2\omega)$ presents a central dip feature, which means that E_z has a hollow radial distribution in the plasma channel, as indicated in Figure 5(c). Note that a hollow structure of the electric field has also been observed using the Stark splitting of OES in [18] and on the electro-optic target deposited by APPJs (i.e. the boundary region) in [28]. This result helps to explain the hollow

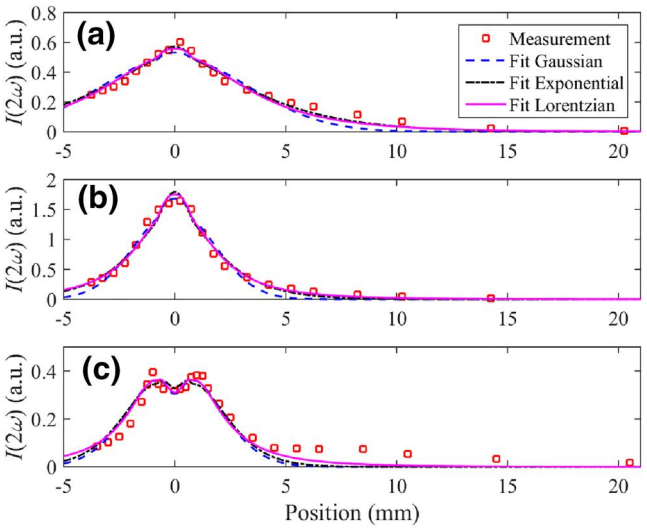

FIGURE 4 The vertical distribution (in the y direction according to Figure 1) of the second harmonic light intensity $I(2\omega)$ near the nozzle of the quartz tube (z = 0 in the axial direction) with a peak voltage of 12 kV and a metal target, from both the measurement and the fitting: (a) 10 ns before the time point when $I(2\omega)$ peaks, (b) the time point when the peak $I(2\omega)$ is reached, (c) 45 ns after the time point when $I(2\omega)$ peaks

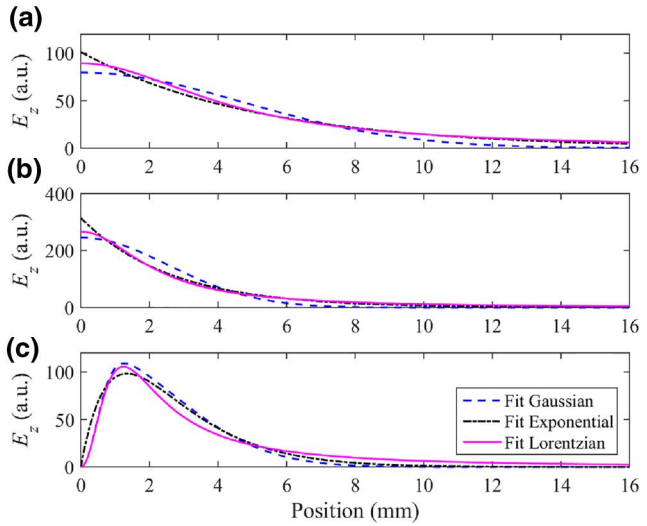

FIGURE 5 The radial distribution of the axial electric field E_z near the nozzle of the quartz tube (z = 0 in the axial direction) with a peak voltage of 12 kV and a metal target, obtained from the fitting of $I(2\omega)$: (a) 10 ns before the time point when $I(2\omega)$ peaks, (b) the time point when the peak $I(2\omega)$ is reached, and (c) 45 ns after the time point when $I(2\omega)$ peaks

(or ring-shape) structure for the radial distribution of the emission intensity in APPJs, which is extensively observed [29], and also confirms the simulated results in [30].

Based on the investigation related to the radial distribution of E_z described above, it can be concluded that due to the dynamic nature of the IW propagation, the radial extent of E_z in APPJs changes on the nanoseconds time scale and the value of peak E_z depends on this distribution corresponding to a same $I(2\omega)$ value. When the axial distribution of E_z is

concerned, ideally, for each axial location and each time point, the radial distribution of E_z should be retraced in order to obtain the value of peak E_z, which is out of the capacity of the current system. Therefore, in the following, a parameter $\langle E_z \cdot x \rangle \propto I(2\omega)^{0.5}/I(\omega)$, based on the calibration result of the E-FISH system with the known and uniform electric field generated by the parallel-plate electrode (i.e. the relationship between $E_0 \cdot L$ and $I(2\omega)^{0.5}/I(\omega)$), is used to demonstrate the IW propagation. The physical meaning of $\langle E_z \cdot x \rangle$ is the line-integrated axial electric field along the laser path, weighted by all factors, including the hyperpolarizabilities of different gas components and the distribution of fundamental laser intensity. Even though two gas components (argon and air) exist and the intensity of second harmonic light is determined by $\chi^{(3)}$ of both gases, the difference between $\chi^{(3)}$[Air] and $\chi^{(3)}$[Ar] is not very huge ($\chi^{(3)}$[Air]/$\chi^{(3)}$[Ar] ≈ 0.79). Therefore, it is safe to argue that the influence of different $\chi^{(3)}$ on $\langle E_z \cdot x \rangle$ is within 20%, considering that the argon flow expands within the tube diameter (1.5 mm) while E_z exists in a wider range of several millimetres. This also partially explains why we choose argon as the operation gas of APPJs in this work (instead of helium which is commonly used in APPJs, with $\chi^{(3)}$[Air]/$\chi^{(3)}$[He] ≈ 22 [26]). Even so, it can still be suspected that the electric field within the argon flow region will contributes more to the final amplitude of $I(2\omega)$ due to both the slightly larger $\chi^{(3)}$[Ar] and the higher fundamental laser density (as the focal point of the laser is within the argon flow region in the experiment). The same approach has been performed in [23, 27], which does not invade the major contents of the current work. Especially, in [27], different gas components also exist in APPJs (nitrogen and air).

Figure 6 shows the measured temporal $\langle E_z \cdot x \rangle$ evolution at different axial locations in the APPJ with a metal target and with a peak voltage of about 12 kV. The nozzle of the quartz tube is at 0 mm and the target is at 21 mm. It can be seen that there is a distinguished two-peak feature for the $\langle E_z \cdot x \rangle$ evolution and the peak $\langle E_z \cdot x \rangle$ is reached later for a position further away from the nozzle, corresponding to the primary and secondary IWs. The value of peak $\langle E_z \cdot x \rangle$ near the nozzle is about 7 (kV/cm)·cm, which gives a peak E_z of about 15 kV/cm based on the fitting results in Figures 4 and 5. As a comparison, the peak E_z value obtained with the E-FISH method is comparable with those from the Stark splitting of OES in [17-19], while it is higher than that from the probes based on the Pockels effect in [20], as the latter method measures the electric field away from the discharge region of the APPJs.

For the first E_z peak, a typical IW feature can be observed [31], i.e. (1) electric field enhancement before the breakdown happens, indicating the approach of the IW front; (2) drastic drop of electric field during the breakdown process, as a result of electron multiplication and shielding effect due to charge separation; (3) weak electric field after the breakdown happens. Note that this weak electric field can explain the formation of the dark region after the luminous head of the APPJ passes by during the propagation of the primary IW (shown in Figure 3), which is not strong enough to give rise to intensive excitation processes, but is still able to drive the current to sustain the discharge propagation. A similar "dip" of the emission

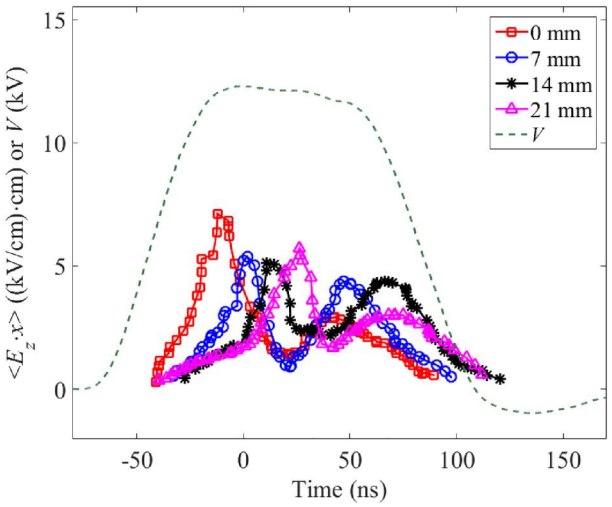

FIGURE 6 The temporal evolution of $\langle E_z \cdot x \rangle$ at different locations in the APPJ with a metal target and with a peak voltage of about 12 kV

intensity is also observed in the fast ionization wave (FIW) discharge propagating in a long tube operated at a moderate pressure in our previous work, in which the drop of the emission intensity after the FIW front passes by shares the same physical mechanism as the dark region in the APPJ [32].

As for the second peak of the electric field, it has a lower peak value but a larger time–width compared with the first one. This feature can explain why there is no dark region during the secondary IW. It is demonstrated that the secondary IW propagates in the conductive channel left from the primary IW [24], i.e. there is a higher pre-ionization degree for the secondary IW. It is also proved in former investigation that a higher pre-ionization degree will decrease the peak electric field at the wavefront region but increases the electric field in the region after the wavefront passes by, turning the profile of the emission intensity from a "dip" feature to a continuously increasing feature [32].

Based on the evolution of the electric field observed above, it can be suspected that the strong electric field at the IW front region can enhance the generation of high-energy electrons, which will further contribute to the formation of active species in APPJs. Similarly, the secondary IW process will reinforce the density of active species (proved by the ever-increasing emission intensity in Figure 3a).

Figure 7(a) and (b) shows the temporal $\langle E_z \cdot x \rangle$ evolution at different locations in the APPJs with a metal target and with a peak voltage of about 10 and 15 kV, respectively. It can be seen that when V_p rises from 10 to 15 kV, the velocity of the primary IW increases significantly from 0.5 to 1.3 mm/ns, which is accompanied with the increase of the average $\langle E_z \cdot x \rangle$ at the wave front from about 5.7 to 6.8 (kV/cm)·cm, showing the correlation between the propagation velocity of APPJs and the peak electric field, i.e. a stronger electric field induced by the higher voltage amplitude (larger potential gradient) will enhance the ionization processes near the IW front region and accelerate the IW propagation [33]. It can also be seen that with a low V_p value of 10 kV, E_z presents a single-peak feature,

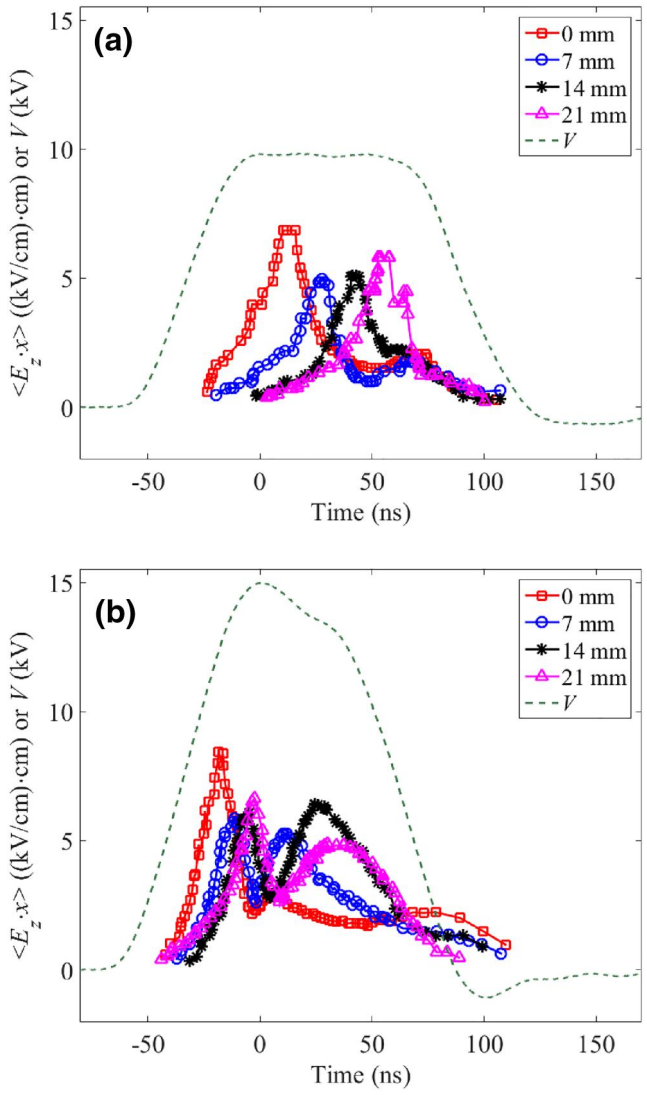

FIGURE 7 The temporal evolution of $<E_z \cdot x>$ at different locations in the APPJ with a metal target: (a) $V_p \approx 10$ kV, (b) $V_p \approx 15$ kV

indicating only one propagation process for the APPJ exists, i.e. there is only primary IW and no secondary IW. The explanation is that in this case the initiation of IW propagation outside the nozzle is later and its propagation velocity is also slower, as a result of which, at the end of the primary IW, the voltage on the HV electrode already turns to the falling edge and cannot maintain a secondary IW propagation. On the contrary, there is a very pronounced secondary IW propagation with $V_p \approx 15$ kV, sustained by the large potential difference between the HV electrode and the ground target at the end of primary IW propagation.

Figure 8(a) and (b) shows the temporal evolution of the $<E_z \cdot x>$ at different locations in the APPJs with the Kapton target and without target (floating), respectively.

With the dielectric target, one noticeable feature is that before HV is applied, there already exists a pronounced electric field, whose value decreases drastically away from the dielectric target, i.e. $<E_z \cdot x> \approx 4.4$ (kV/cm)·cm near the target (at 21 mm) and $<E_z \cdot x>$ drastically drops to 1.4 (kV/cm)·cm at 7 mm away from the target. This electric field is due to the existence of residual charges on the dielectric surface left-over by the previous pulse. Indeed, by using a Kelvin electrostatic probe and performing an off-line measurement (as has performed in [14]), it is verified that the residual surface potential of the dielectric at around one minute after the discharge is around 2–3 kV (positive). This means that the polarity of the surface charges deposited by the APPJ is the same as the HV polarity and the direction of the electric field generated by the residual surface charges is in the opposite direction to that during IW propagation. Therefore, the electric field is reversed before and after the HV duration in Figure 8(a) and the flip point is chosen to be the local minimum value, similar as [14, 16]. Notice that the significant sign-reversal "jumps" in this figure, which do not occur in reality, is explained by both the limited spatial resolution (~ 260 μm in the direction perpendicular to the laser beam) and temporal resolution (laser pulse width ≈ 7–9 ns plus jitter between laser and HV pulse ≈ 8 ns) of the E-FISH system used in current work and the intensity of the second harmonic light does not decrease to zero in the measurement.

As for the free APPJ without a target, the velocity of the primary IW is slower compared with the cases with a target, which is consistent with the discharge images. A distinguished difference is related to the second E_z peak. In the free APPJ, the second E_z peak is the strongest near the nozzle and decays away from the nozzle. In contrast, with a target, it is stronger away from the nozzle (as shown in Figures 6 and 7). In addition, the second E_z peak in the free APPJ appears during the voltage falling edge, while the second E_z peak in the APPJ with a target appears during the voltage plateau. Note that there is no second propagation during the voltage falling edge in the APPJ with a metal target under a low peak voltage (shown in Figure 7a). On the basis of these two points of difference, it is reasonable to argue that the mechanism underlying the secondary propagation process in the APPJ without a target is different from the secondary IW. In a free APPJ case, during the voltage falling edge, the electrons are supplied toward the head of the jet (where positive ions are left over during the first propagation process) under a reversed electric field.

4 | SUMMARY AND CONCLUSIONS

The study has used E-FISH method to measure the temporal evolution and spatial distribution of the axial electric field in the nanosecond pulsed APPJs. Temporally resolved optical imaging is used to visualize the APPJ propagation process. Combining both methods, it is verified that IW exists during the APPJ development, i.e. the movement of luminous APPJ head is accompanied with the propagation of IW front indicated by the peak electric field.

Importantly, it is found that before the (primary) IW front arrives, the radial distribution of E_z presents a central-peak

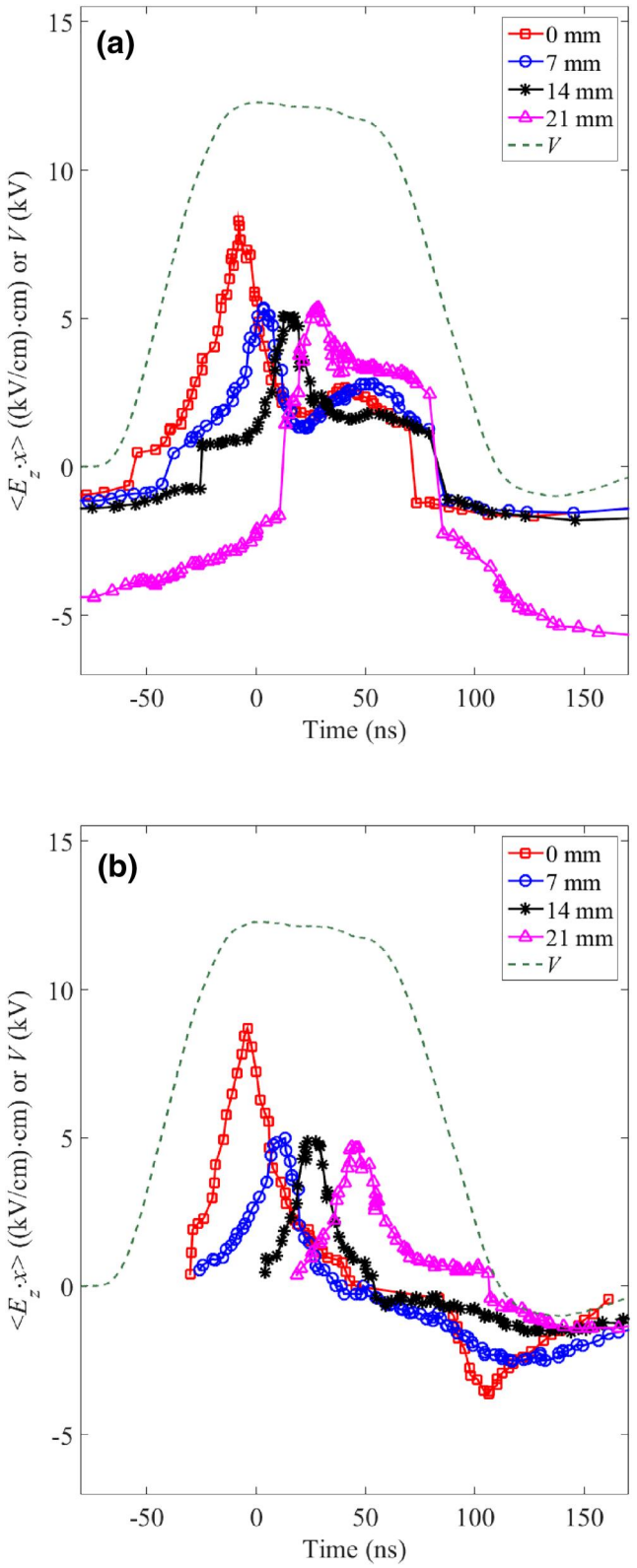

FIGURE 8 The temporal evolution of $<E_z \cdot x>$ at different locations in the APPJs with a peak voltage of about 12 kV: (a) with the Kapton target and (b) with no target (free APPJ)

profile and the radial expansion of E_z decreases as the IW front approaches. However, after the (primary) IW front passes by, i.e. in the plasma channel, E_z has a hollow radial distribution. In addition, with the increase of the peak voltage, both the IW propagation velocity and the peak electric field at the wave front region increase. The single-peak feature of the electric field under a low peak voltage transfers to the double-peak feature under a higher peak voltage, indicating the existence of both primary and secondary IWs.

The influence of target conditions on the electric field evolution in the APPJs is also investigated. In the metal target cases, there is no residual electric field before the HV pulses are imposed. In the APPJ with a dielectric target, the residual surface charges generate a background electric field in the opposite direction to that during IW propagation. While in the free APPJ without a target, on the voltage falling edge, a negative electric field drives the electron flow to compensate the positive ions left over during the forward IW propagation on the voltage rising edge.

ACKNOWLEDGMENTS

This work was supported by the National Science Fund for Distinguished Young Scholars (Grant No. 51925703), the National Natural Science Foundation of China (Grant Nos. 51637010, 51777204, 51907190, and 52011530026), and the Royal Society – Newton Advanced Fellowship, UK (Grant No. NAF\R2\192117).

The authors are grateful to Prof. Igor Adamovich from Ohio State University, who worked with the build-up of the E-FISH system in June 2018, supported by the Chinese Academy of Sciences President's International Fellowship Initiative under contract 2018VEA0004.

ORCID

Bangdou Huang https://orcid.org/0000-0002-1523-7380
Cheng Zhang https://orcid.org/0000-0003-1512-2820
Tao Shao https://orcid.org/0000-0002-5738-1241

REFERENCES

1. Chiang, W., et al.: Microplasmas for advanced materials and devices. Adv. Mater. 32, 1905508 (2020)
2. Lu, X.P., et al.: Reactive species in non-equilibrium atmospheric-pressure plasmas: Generation, transport, and biological effects. Phys. Rep. 630, 1–84 (2016)
3. Shao, T., et al: Atmospheric-pressure pulsed discharges and plasmas: mechanism, characteristics and applications. High Volt. 3, 14–20 (2018).
4. Thomson, J.J.: Researches in Electricity and Magnetism, pp. 115. Clarendon Press, Oxford (1893)
5. Takashima, K., et al.: Experimental and modeling analysis of fast ionization wave discharge propagation in a rectangular geometry. Phys. Plasmas. 18, 083505 (2011)
6. Huang, B.D., et al.: The dynamics of discharge propagation and x-ray generation in nanosecond pulsed fast ionisation wave in 5 mbar nitrogen. Plasma Sources Sci. Technol. 28, 095001 (2019)
7. Lu, X.P., Ostrikov, K.: Guided ionization waves: The physics of repeatability. Appl. Phys. Rev. 5, 031102 (2018)

8. Zhang, M., et al.: Measurement of transient electron density of a pulsed microwave argon plasma jet via microwave Rayleigh scattering. J. Appl. Phys. 128, 123301 (2020)
9. Dogariu, A., et al: Species-independent femtosecond localized electric field measurement. Phys. Rev. Appl. 7, 024024 (2017)
10. Goldberg, B.M., et al.: 1D time evolving electric field profile measurements with sub-ns resolution using the E-FISH method. Opt. Lett. 44, 3853 (2019)
11. Retter, J.E., Elliott, G.S.: On the possibility of simultaneous temperature, species, and electric field measurements by coupled hybrid fs/ps CARS and EFISHG. Appl. Opt. 58, 2557 (2020)
12. Chng, T.L., et al.: Electric field evolution in a diffuse ionization wave nanosecond pulse discharge in atmospheric pressure air. Plasma Sources Sci. Technol. 28, 09LT02 (2019)
13. Cui, Y.Z., Zhuang, C.J., Zeng, R.: Electric field measurements under DC corona discharges in ambient air by electric field induced second harmonic generation. Appl. Phys. Lett. 115, 244101 (2019)
14. Huang, B.D., et al.: Surface ionization wave propagation in the nanosecond pulsed surface dielectric barrier discharge: the influence of dielectric material and pulse repetition rate. Plasma Sources Sci. Technol. 29, 044001 (2020)
15. Chng, T.L., et al.: Electric field induced second harmonic (E-FISH) generation for characterization of fast ionization wave discharges at moderate and low pressures. Plasma Sources Sci. Technol. 28, 045004 (2019)
16. Orr, K., et al.: Measurements of electric field in an atmospheric pressure helium plasma jet by the E-FISH method. Plasma Sources Sci. Technol. 29, 035019 (2020)
17. Olszewski, P., et al.: Measurement and control of the streamer head electric field in an atmospheric-pressure dielectric barrier plasma jet. Plasma Sources Sci. Technol. 23, 015010 (2014)
18. Sretenović, G.B., et al.: Spectroscopic measurement of electric field in atmospheric-pressure plasma jet operating in bullet mode. Appl. Phys. Lett. 99, 161502 (2011)
19. Sretenović, G.B., et al.: Spatio-temporally resolved electric field measurements in helium plasma jet. J. Phys. D: Appl. Phys. 47, 102001 (2014)
20. Darny, T., et al.: Analysis of conductive target influence in plasma jet experiments through helium metastable and electric field measurements. Plasma Sources Sci. Technol. 26, 045008 (2017)
21. Huang, B.D., et al.: The influence of the voltage rise rate on the breakdown of an atmospheric pressure helium nanosecond parallel-plate discharge. J. Phys. D Appl. Phys. 48, 125202 (2015)
22. Viegas, P., et al.: Interaction of an atmospheric pressure plasma jet with grounded and floating metallic targets: simulations and experiments. Plasma Sources Sci. Technol. 29, 095011 (2020)
23. Adamovich, I.V., et al.: Nanosecond second harmonic generation for electric field measurements with temporal resolution shorter than laser pulse duration. J. Phys. D Appl. Phys. 53, 145201 (2020)
24. Babaeva, N.Y., et al.: Plasma bullet propagation and reflection from metallic and dielectric targets. Plasma Sources Sci. Technol. 28, 095006 (2019)
25. Chng, T.L., Starikovskaia, S.M., Schanne-Klein, M.C.: Electric field measurements in plasmas: how focusing strongly distorts the E-FISH signal. Plasma Sources Sci. Technol. 29(12), 125002 (2020)
26. Shelton, D.P., Rice, J.E.: Measurements and calculations of the hyperpolarizabilities of atoms and small molecules in the gas phase. Chem. Rev. 94, 3–29 (1994)
27. van der Schans, M., et al.: Electric field measurements on plasma bullets in N2 using four-wave mixing. Plasma Sources Sci. Technol. 26, 115006 (2017)
28. Viegas, P., et al.: Investigation of a plasma–target interaction through electric field characterization examining surface and volume charge contributions: modeling and experiment. Plasma Sources Sci. Technol. 27, 094002 (2018)
29. Chang, Z.S., et al.: Plasma "bullet" with hollow structure: formation and evolution. Sci. Rep. 8, 7599 (2018)
30. Lazarou, C., et al.: Numerical simulation of capillary helium and helium−oxygen atmospheric pressure plasma jets: propagation dynamics and interaction with dielectric. Plasma Sources Sci. Technol. 27, 105007 (2018)
31. Naidis, G.V., Babaeva, N.Y.: Electric field distributions along helium plasma jets. High Volt. 5, 650–653 (2020)
32. Huang, B.D., et al.: The effect of the pulse repetition rate on the fast ionization wave discharge. J. Phys. D Appl. Phys. 51, 225202 (2018)
33. Naidis, G.V.: Positive and negative streamers in air: Velocity-diameter relation. Phys. Rev. E. 79, 057401 (2009)

How to cite this article: Huang, B., et al.: Ionization waves in nanosecond pulsed atmospheric pressure plasma jets in argon. High Volt. 6(4), 665–673 (2021). https://doi.org/10.1049/hve2.12067